

# Overview of Spark Plasma Texturing of Functional Ceramics

Jacques G. NOUDEM <sup>\*</sup> and Yiteng XING

École Nationale Supérieure d'Ingénieurs de Caen, Université de Caen Normandie, CNRS, CRISMAT, 14000 Caen, France; yiteng.xing@ensicaen.fr

\* Correspondence: jacques.nouDEM@ensicaen.fr

**Abstract:** This work reports the progress in the preparation of superconducting and thermoelectric lamellar compounds processed by the unconventional Spark Plasma Sintering (SPS). The SPS equipment was modified with the aim of obtaining the textured and dense superconductor  $\text{Bi}_2\text{Sr}_2\text{Ca}_2\text{Cu}_3\text{O}_{10}$ , *p*-type oxide thermoelectric bulk as  $\text{Ca}_3\text{Co}_4\text{O}_9$  and  $\text{Ca}_{3-x}\text{Ag}_x\text{Co}_4\text{O}_9$ /Ag composites respectively. The new process is referred to as Spark Plasma Texturing (SPT). During SPT, the bulk material can freely deform. As a result, inter-grain preferential crystallographic orientation is created. The series of sintered and textured samples using the same Ag content were processed respectively. From the results, we can evidence: (i) the magnetic and/or structural transition around 350 °C, for both series of samples. (ii) The electrical resistivity ( $\rho$ ) decreases with increasing Ag-substituted or Ag-added. (iii) The Seebeck coefficient ( $S$ ) of the textured series is higher than that of the sintered series. In the case of the Ag-substituted,  $S$ , decreases with Ag content. The optimized composite is found to be  $\text{Ca}_{2.6}\text{Ag}_{0.4}\text{Co}_4\text{O}_9$ /8wt% Ag. We can note the remarkable reduction of  $\rho$ , and the improvement of power factor values up to  $360 \mu\text{W}\cdot\text{m}^{-1}\cdot\text{K}^{-2}$ . The superconducting properties of single phased  $\text{Bi}_2\text{Sr}_2\text{Ca}_2\text{Cu}_3\text{O}_{10}$  ( $\text{Bi}2223$ ) consolidated using SPS and SPT will also be discussed.

**Keywords:** superconductor  $\text{Bi}_2\text{Sr}_2\text{Ca}_2\text{Cu}_3\text{O}_{10}$ ; thermoelectric  $\text{Ca}_3\text{Co}_4\text{O}_9$ ;  $\text{Ca}_{2.6}\text{Ag}_{0.4}\text{Co}_4\text{O}_9$ /Ag composite; spark plasma sintering; texturing



**Citation:** NOUDEM, J.G.; XING, Y. Overview of Spark Plasma Texturing of Functional Ceramics. *Ceramics* **2021**, *4*, 97–107. <https://doi.org/10.3390/ceramics4010009>

Academic Editors: Gilbert Fantozzi, Koji Morita and Manuel Belmonte

Received: 19 January 2021  
Accepted: 10 March 2021  
Published: 15 March 2021

**Publisher's Note:** MDPI stays neutral with regard to jurisdictional claims in published maps and institutional affiliations.



**Copyright:** © 2021 by the authors. Licensee MDPI, Basel, Switzerland. This article is an open access article distributed under the terms and conditions of the Creative Commons Attribution (CC BY) license (<https://creativecommons.org/licenses/by/4.0/>).

## 1. Introduction

Since the discovery of the High-Temperature Superconductivity (HTS) in  $\text{BaLaCuO}$  [1], it is well-known that to obtain the significant critical current densities in HTS polycrystalline materials, grain alignment is necessary. The oxide  $\text{BiSrCaCuO}$  ceramics seems to be one of the promising candidates for superconducting applications. Different ways have been used to fabricate the materials with the oriented grains such as: (i) solidification in the thermal gradient or under a high magnetic field [2–4], (ii) the hot isostatic pressing (HIP) process [5,6] where the defects induce under pressure [7] were also attributed to the enhancement of the critical current. (iii) The uniaxial pressing technique, where the combination of the grains alignment and with better connectivity between them improves the transport properties [8–10].

On the other hand, the discovery of large thermopower in  $\text{NaCo}_2\text{O}$  [11] has contributed considerably to the development of other layered cobalt oxides such as:  $\text{Ca-Co-O}$ ,  $\text{Bi-Ca/Sr-Co-O}$  and  $\text{Bi-Pb-Sr-Co-O}$  [12,13]. All these systems shown large thermoelectric power and exhibit a figure of merit,  $ZT = S^2T/\rho k$  ( $S$  is Seebeck coefficient,  $T$  temperature,  $\rho$  electrical resistivity and  $k$  the thermal conductivity) varying from 0.2 to 1.2. The oxide thermoelectric materials seem to be an alternative for practical applications at high temperatures as compared to the conventional semiconducting  $\text{Bi}_2\text{Te}_3$  or  $\text{SiGe}$  materials [14,15].

The processing methods are very important to obtain the polycrystalline with the desired microstructure. To improve thermoelectric properties, substantial work has been done such as partial substitutions of Sr, La on the Ca site and/or and Cu on the Co site [13,16–19], hot-pressing [13,15,20], reactive templated grain growth [21], magnetic texturisation or spark plasma sintering [13,22] in order to exploit the intrinsic anisotropy

or crystallographic anisotropy of Co-based oxide materials during processing. For hot-pressing and magnetic texturisation processes, the reports are more related on BiCaCoO, BiPbSrCoO phases where the presence of bismuth seems to be helpful for partial melting which is favorable to the orientation of the crystallites.

In this work, we employed Spark Plasma Sintering (SPS) set-up to streamline the grain texture of both superconductor  $\text{Bi}_2\text{Sr}_2\text{Ca}_2\text{Cu}_3\text{O}_{10}$  (Bi2223) and thermoelectric  $\text{Ca}_3\text{Co}_4\text{O}_9$  (Co349) or  $\text{Ca}_{2.6}\text{Ag}_{0.4}\text{Co}_4\text{O}_9$  (Co349/Ag) composite ceramics. The SPS was modified so as to obtain textured lamellar compounds. The new process is referred to as Spark Plasma Texturing (SPT). During SPT, the bulk material can freely deform itself. As a result, inter-grain preferential crystallographic orientation is favored. The correlations between the microstructures generated and the functional properties of both superconductor (Bi2223) and thermoelectric (Co349) using SPS and SPT were investigated and will be discussed in detail. This article is structured as follows: after the introduction, the experimental conditions will be detailed followed by the analysis of the results in section three and finally the conclusion.

## 2. Experimental

### 2.1. Samples Preparation and Processing Conditions

In this section, three sets of ceramic powders were processed: (i) commercial superconducting  $\text{Bi}_2\text{Sr}_2\text{Ca}_2\text{Cu}_3\text{O}_{10}$  (Bi2223) (SSC Neyco 3N, purity 99.9%, particle size of 2  $\mu\text{m}$ ), (ii) thermoelectric (TE)  $\text{Ca}_3\text{Co}_4\text{O}_9$  (Co349) and (iii) thermoelectric  $\text{Ca}_{2.6}\text{Ag}_{0.4}\text{Co}_4\text{O}_9$  (Co349/Ag) composites. The TE ceramic powders were prepared by first calcining a stoichiometric mixture of commercially available (purity  $\approx 99\%$ ),  $\text{Co}_3\text{O}_4$ ,  $\text{Ag}_2\text{O}$ , oxides and  $\text{CaCO}_3$  carbonate at 900 °C for 12 h. Then, the powder was refined (particle size  $\approx 1 \mu\text{m}$ ) by regrinding. The pellets with 10 mm diameter of both powders were formed by uni-axial pressure (30 MPa) at room temperature in order to obtain a relatively dense raw material free of microcracks. These pellets were pre-sintered at 500 °C and 700 °C for Bi2223 and Co349 respectively for 2 h for mechanical reasons before the Spark Plasma Texturing (SPT) [23]. The pre-sintered sample was placed at the center of graphite die of 20 mm diameter or tungsten carbide-WC die (15 mm diameter) in order to ensure the free deformation (Figure 1b) and grains alignment of the sample. The final processing was carried out using the SPS system under a dynamic vacuum ( $10^{-3}$  bar). In another configuration, the ceramic powder was directly introduced into the graphite (Figure 1a) mold as reported elsewhere [24]. The FCT-HP D25 (Rauenstein, Germany) SPS machine was used in DC mode with a maximal power of 8 kW, a heating and cooling rate of 100° /min. The processing conditions for the thermoelectric materials are 900 °C with pressure of 50 MPa and dwell time of 20 min. In order to investigate the anisotropic properties, several discs of Co349 (Figure 2a) were prepared by SPT, then polished and hot-stacked (Figure 2b) without any binder. In addition, to avoid the reduction of the oxygen content on the superconducting Bi2223 oxide, the powder was introduced into the tungsten carbide (WC) die, then placed into the working chamber in an air atmosphere at 600 °C under 300 to 500 MPa for 20 min.

### 2.2. Characterization

XRD measurements were investigated on a 4-circles X'PERT Philips goniometer in the Bragg-Brentano geometry. Carl Zeiss Supra 55 (Oberkochen, Germany) high-resolution scanning electron microscope (SEM) equipped with EDS was used to investigate the microstructure and the chemical composition of the samples after processing. A commercial SQUID (Quantum Design) magnetometer was used for magnetization measurements. Finally, the electrical resistivity,  $\rho$ , and thermoelectric power or Seebeck coefficient,  $S$ , were measured simultaneously by the dc four-probe method by using a ZEM-3 (ULVAC-RIKO, Inc., Yokohama, Japan) from room temperature to 750 °C.

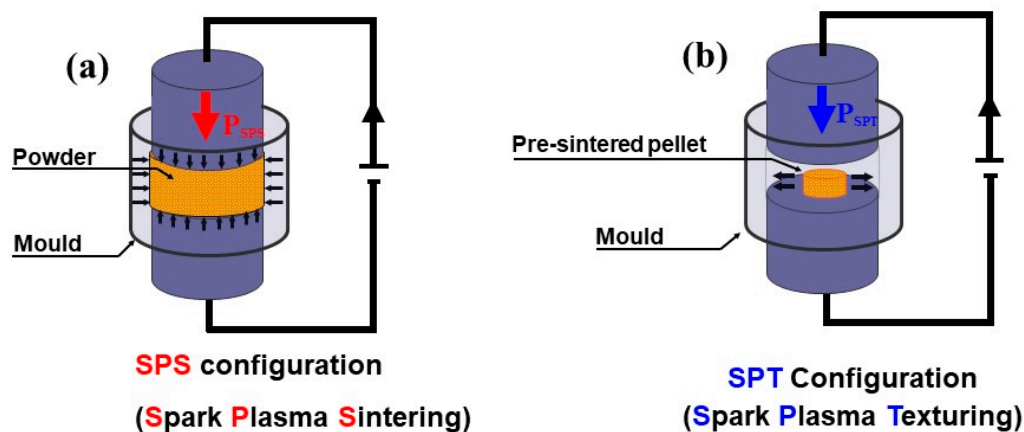


Figure 1. (a) Conventional Spark Plasma Sintering (SPS) configuration and the (b) new Spark Plasma Texturing [24].

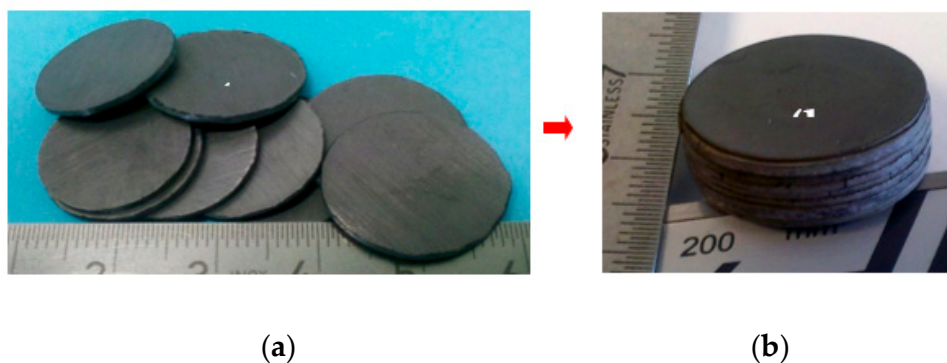


Figure 2. (a) As-processed and (b) hot-stacked Co349 pellet samples.

### 3. Results and Discussion

In this section, the results regarding three ceramic oxides will be discussed:

- (i) Superconducting  $\text{Bi}_2\text{Sr}_2\text{Ca}_2\text{Cu}_3\text{O}_{10}$  (Bi2223)
- (ii) Thermoelectric  $\text{Ca}_3\text{Co}_4\text{O}_9$  (Co349)
- (iii) Thermoelectric  $\text{Ca}_{3-x}\text{Ag}_x\text{Co}_4\text{O}_9/\text{Ag}$  (Co349/Ag) composites

#### 3.1. Thermoelectric $\text{Ca}_3\text{Co}_4\text{O}_9$ (Co349)

X-ray diffraction of the face perpendicular and parallel to the applied pressure direction during processing is shown on Figure 3. The patterns show the single-phase nature of the powders with no secondary or impurity phases. All the peaks were indexed as on XRD patterns of conventional sintering samples reported elsewhere [25]. This indexing including satellite reflections originated from the misfit-layered structure was made according to some [26,27] reported works. The faces perpendicular to the applied pressure (SPS<sup>⊥</sup> and SPT<sup>⊥</sup> samples) reveal strong (00 $\ell$ ) reflections, in contrast to the faces parallel to the applied pressure (SPS<sup>//</sup> and SPT<sup>//</sup> samples) where more peaks are (hk0) or non-sample showing all (hk $\ell$ ) diffraction peaks [25]. This shows that the experimental process tends to align the crystallographic c-axis of platelets following the preferential axial direction. These features can be correlated with the following microstructures.

Figure 4 shows the SEM micrographs of the reference sample, in other words, the sample prepared by conventional sintering (CS). Then, 98% dense SPS and SPT samples. It shows essentially the faces fractured parallel and perpendicular to the pressure applied during sintering. For the CS sample, the grains are randomly distributed and loosely assembled (Figure 4a). In this case, the sample density is only 60% of the theoretical value [12,28]. The SEM picture of the SPS sample (Figure 4b) shows no preferential grain

orientation, with respect to the SPT sample (Figure 4c). The SPT sample shows the high degree of orientation of large platelets compactly stacked up along the applied pressure axis (Figure 4c). The comparison of Figure 4b and c demonstrates the detrimental influence of the walls of the shaping mold on the morphology of these layer structure materials. In fact, the microstructure of the SPT sample is similar to the one usually obtained with the hot-forging/pressing (HP) process [29–31]. Nevertheless, the HP requires days to prepare the sample, with respect to about an hour with SPT. We can conclude that the Spark Plasma Texturing (SPT) is favorable for grain growth and allows inducing good alignment among the grains, required for improved functional properties of the bulk material.

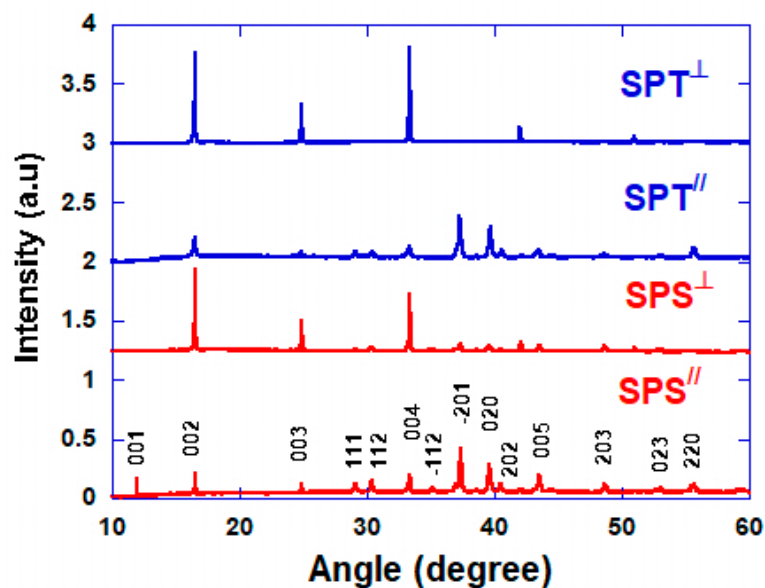


**Figure 3.** XRD diffraction curves were obtained, from the faces perpendicular and parallel to the applied pressure during Spark Plasma Sintering (SPS, red color) and Spark Plasma Texturing (SPT, blue color).

The temperature ( $T$ ) dependence of the resistivity ( $\rho$ ) for the reference  $\text{Ca}_3\text{Co}_4\text{O}_9$  sample ( $\sigma = 0$  MPa), and the samples processed by SPS and SPT respectively is shown in Figure 5a. What can be deduced from it? The  $\rho(T)$  curves show similar behavior, with the magnetic transition around 250 °C. This is in agreement with some reports [12,25] on thermoelectric oxides. These curves show that at 100 °C, the resistivity of the non-pressed sample is 37 m $\Omega$ .cm as compared to 17 and 7 m $\Omega$ .cm for the SPS and SPT samples respectively. The decrease in resistivity values can be considered as being due to the densification of the material under pressure and good alignment between grains. For the thick SPS and hot stacked SPT samples, the electrical resistivities (Figure 5b) have been measured in parallel and perpendicular directions to the applied pressure during sample processing. As expected, the electrical resistivity of the samples processed by Spark Plasma Sintering and Texturing exhibit a high anisotropy than the SPS one. At 150 °C, we can deduce a ratio of  $\rho_{\text{SPT}\parallel} / \rho_{\text{SPT}\perp} = 7$  for SPT compare to  $\rho_{\text{SPS}\parallel} / \rho_{\text{SPS}\perp} \sim 2$  for SPS sample. This is well correlated to the microstructure shown in Figure 4 where the SPT exhibits strong alignment of platelets where the current can flow easily and lead to the low in-plane resistivity ( $\rho_{\text{SPT}\perp}$ ).

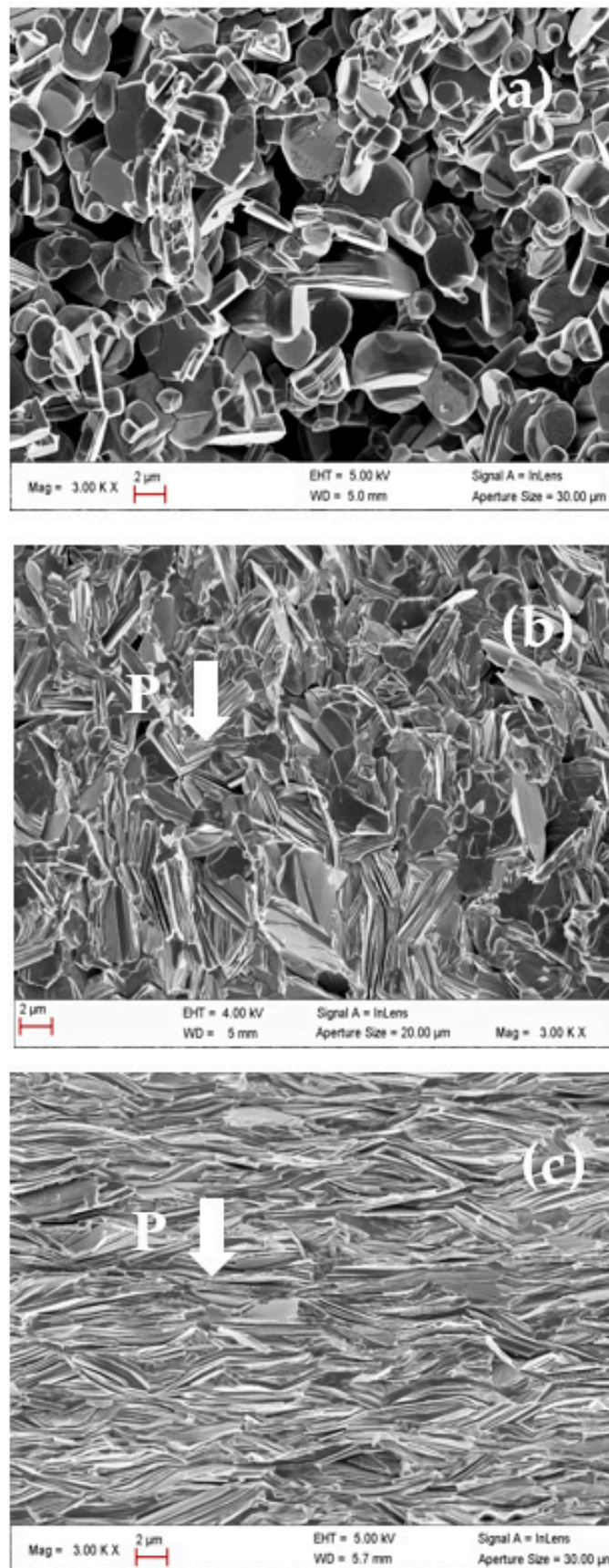


**Figure 4.** SEM micrographs of the  $\text{Ca}_3\text{Co}_4\text{O}_9$  *p*-type thermoelectric (a) Conventional Sintered (CS), (b) Spark Plasma Sintering sample, fractured surfaces parallel to applied pressure (P) and (c) Spark Plasma Texturing (SPT) sample.

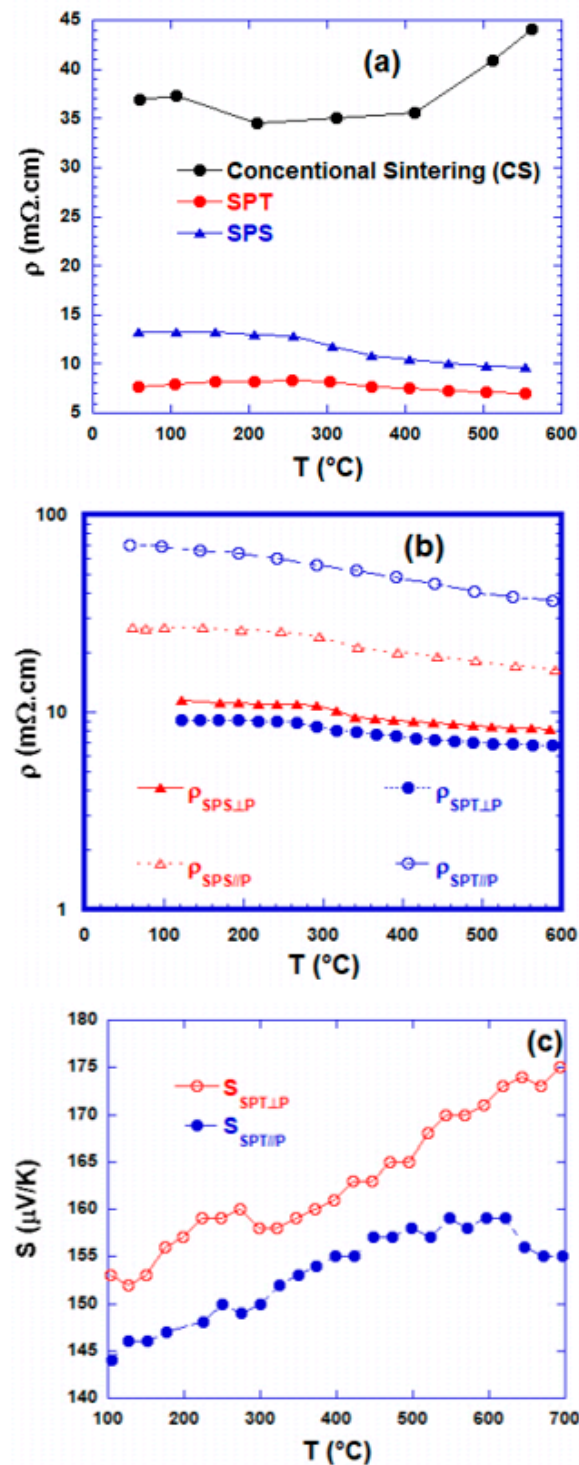


**Figure 5.** (a) Temperature dependence of the electrical resistivity on the conventional sintering (CS) sample, compared to in-planes SPS and SPT samples. (b) Temperature dependence of the electrical resistivity of in and out-planes samples processed by SPS and SPT respectively. (c) Temperature dependence of in and out-planes Seebeck coefficient for sample processed by SPT.

In addition, the Seebeck coefficient,  $S$  or thermoelectric power versus temperature is illustrated on Figure 5c and shows *p-type* thermoelectric material within the explored temperature range. This *p-type* behavior indicates that the hole carriers dominate the transport properties. On the other hand, the thermoelectric power is insensitive to grain orientation. The values measured in both directions are quite close. An explanation of

the anisotropic behavior seems to be related to the tensorial expression [31] of the Seebeck coefficient showing that the in-planes (ab-planes) component is more pronounced than the out-of-the plane (c-axis). Some authors [32,33] reported the anisotropic thermopower in a misfit-layered calcium cobaltite. An explanation is  $S(T)$  has two components  $S_{tr}(T)$  and  $S_{\mu}(T)$ . Where  $S_{tr}(T)$  is the transport term and  $S_{\mu}(T)$  the entropic term. The transport term is probably higher than the entropic one in the case of dc four-probe method measurements.

### 3.2. Thermoelectric $Ca_{3-x}Ag_xCo_4O_9/Ag$ (Co349/Ag) Composites

The high-temperature thermoelectric properties of 349/Ag composite were optimized by combining the substitution of  $Ag^+$  with  $Ca^{2+}$  or Ag-added and spark plasma sintering (SPS) consolidation. A series of sintered samples using various Ag content was processed respectively. The bulk densities of all samples are about 98% of the theoretical densities. From the results, we can evidence the effect of silver doping on thermoelectric properties. This is related to the change of the carrier concentrations.

Figure 6a shows: (i) the magnetic and/or structural transition around 350 °C, for the series of samples. (ii) The electrical resistivity ( $\rho$ ) decreases with increasing Ag-substituted or Ag-added. (iii) A low resistivity value  $\sim 2$  m $\Omega$ .cm over the entire temperature range is found when the Ca is substituted with  $x = 0.8$  silver (Ag). The decrease of electrical resistivity with the Ag content can be argued as a result of the change of the carrier density with doping [34,35].

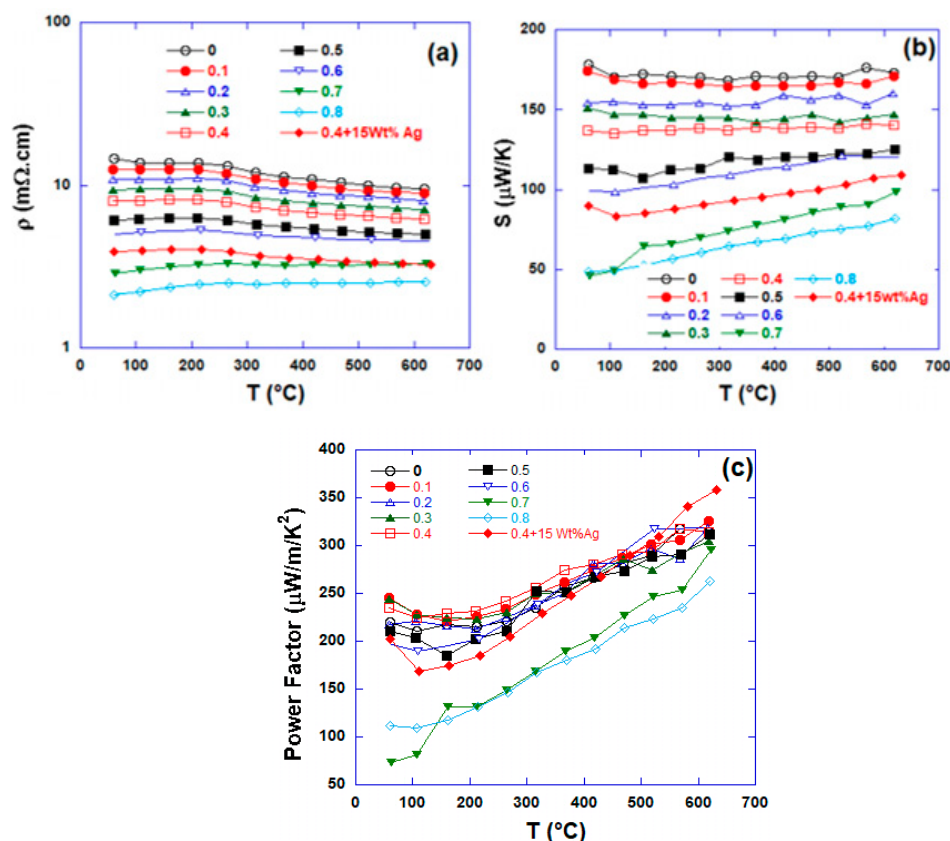


**Figure 6.** Temperature dependence of thermoelectric properties (a) electrical resistivity, (b) Seebeck coefficient and (c) Power factor of  $Ca_{3-x}Ag_xCo_4O_9/Ag$  composites.

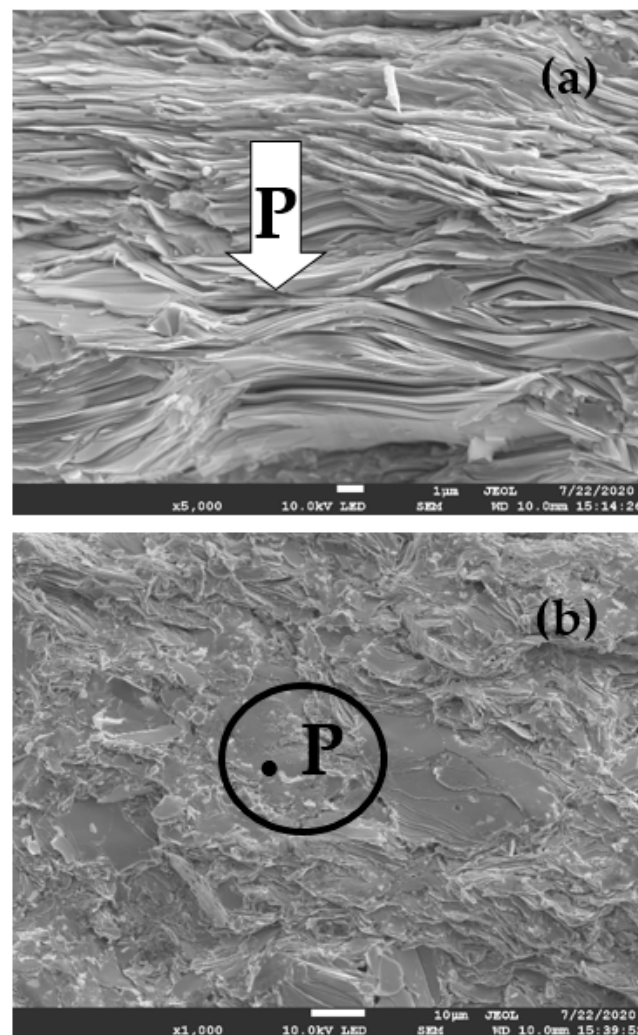
In this study, a fraction of the divalent  $Ca^{2+}$  has been substituted by the monovalent  $Ag^+$ , which could modify the transport and thermoelectric properties of polycrystalline  $Ca_{3-x}Ag_xCo_4O_9/Ag$ .

Figure 6b shows the temperature and Ag content dependencies of the thermoelectric powers or Seebeck coefficients,  $S$  of the samples. As expected,  $S$  decreases with

increasing Ag content. Basically, the thermoelectric power depends on the chemical composition of the material. The fraction of  $\text{Co}^{4+}$  holes on the Co sites in the  $\text{CoO}_2$  layers change progressively with Ag content and systematically induce the modification in the thermoelectric power according to the Heikes formula [36]. The optimized composite is found to be  $\text{Ca}_{2.6}\text{Ag}_{0.4}\text{Co}_4\text{O}_9/15\text{wt}\% \text{Ag}$ . We can note the remarkable reduction of  $\rho$ , and an improvement of power factor (Figure 6c) value up to  $360 \mu\text{W}\cdot\text{m}^{-1}\cdot\text{K}^{-2}$  compared to  $314 \mu\text{W}\cdot\text{m}^{-1}\cdot\text{K}^{-2}$  and  $260 \mu\text{W}\cdot\text{m}^{-1}\cdot\text{K}^{-2}$  respectively for un-doped sample and sample with Ag content  $x = 0.1$ .

### 3.3. $\text{Bi}_2\text{Sr}_2\text{Ca}_2\text{Cu}_3\text{O}_{10}$ Superconductor

The microstructure of the sample prepared by SPT is shown in Figure 7a. The fractured cross-section is evidenced. We can observe a high degree of orientation of large platelets compactly stacked (98% relative density) along the stress direction. This stands in contrast to non-pressed samples [37] in which much smaller platelets appear to be randomly distributed and loosely assembled, resulting in a weak relative density (60%). The microstructural aspects for the textured sample clearly show an increase in elongated platelet size ( $6 \mu\text{m}$ ) and a decrease in the voids between the grain boundaries. Figure 7b shows the SEM of the face broken perpendicular to the applied annealing pressure. In contrast to the parallel direction, the large grains with the surface parallel to the applied pressure are evidenced.



**Figure 7.** SEM micrograph pictures of the face cleaved (a) parallel to the pressure (P) axis for the Bi2223 sample processed SPT. (b) Surface perpendicular to the applied pressure (P).

Figure 8a shows magnetic moment versus temperature curve. It can be seen as expected, the critical temperature,  $T_c \approx 110$  K. The large transition width ( $\Delta T$ ) can attribute to the presence of some phases: Bi2212, 14:24 and/or Bi3221 as reported elsewhere [38]. Figure 8b shows the magnetic hysteresis,  $M$  (H) cycles measured carried out on a  $3 \times 3 \times 3$  mm<sup>3</sup> specimen cut out from a bulk sample. The excitation field,  $H$  is either parallel or perpendicular to the direction of the pressure,  $P$ , applied during processing. The hysteresis of the cycle measured with  $H$  parallel to the stress direction is larger than that of the other cycle ( $\Delta M_{H//c} > \Delta M_{H\perp c}$ ). At the self field, the magnetic moment anisotropy ratio is around 3. This can be correlated to the micrographs, confirming the texture of the bulk sample with the preferential crystallographic of the grains.

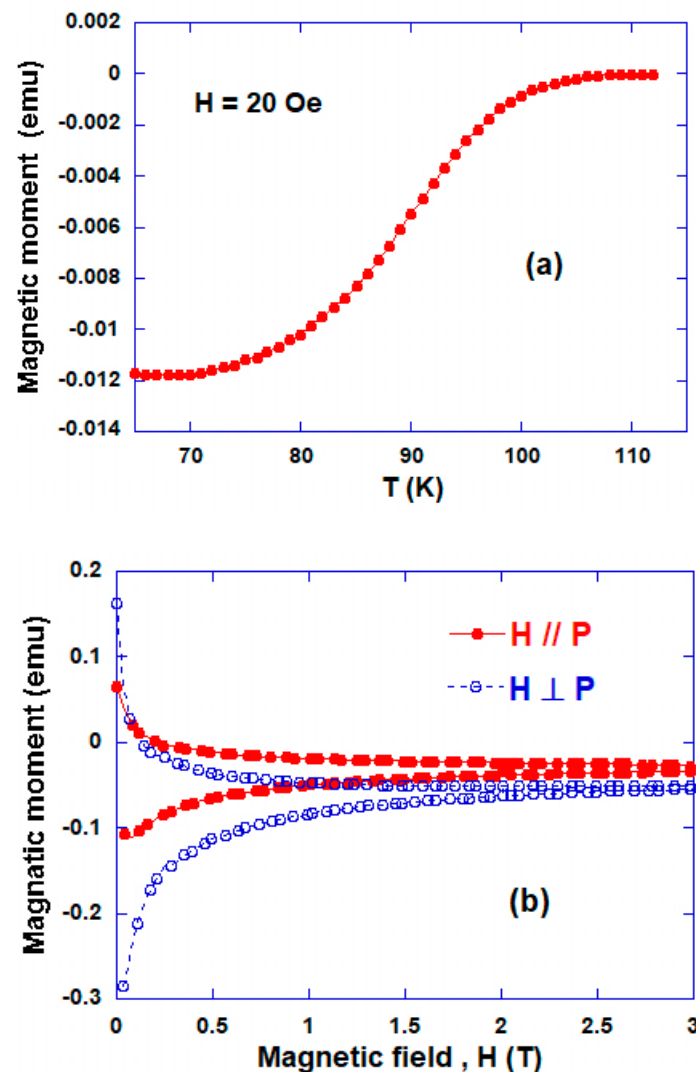


**Figure 8.** (a) Temperature dependence of magnetic moment. (b) Magnetization hysteresis cycles at 20 K with the measuring field  $H$ , parallel (o) and perpendicular (●) to the pressure applied during processing.

#### 4. Conclusions

To sum up, highly textured dense functional ceramics with grain-alignment have been successfully processed. The resistivity in the out of the planes was close to height orders of magnitude larger than the in-plane resistivity for the SPT *p-type*  $\text{Ca}_3\text{Co}_4\text{O}_9$ . Crystallite alignment is effective in lowering the electrical resistivity which could be useful in improving the figure of merit parameter. Further investigations such as thermal conductivities in order to estimate the figure of merit seem meaningful. The thermoelectric  $\text{Ca}_{3-x}\text{Ag}_x\text{Co}_4\text{O}_9/\text{Ag}$

composites were prepared by SPS. The effect of the silver doping on the thermoelectric properties was evidenced. The optimum composition  $\text{Ca}_{2.6}\text{Ag}_{0.4}\text{Co}_4\text{O}_9/15\text{wt}\%$  Ag has been formulated with a high power factor of  $360 \mu\text{W}\cdot\text{m}^{-1}\cdot\text{K}^{-2}$ . Furthermore, the substitution of  $\text{Ca}^{2+}$  by a monovalent heavy-ion such as  $\text{Ag}^+$  can lead to an increase in the diffusion of crystal defects and impurities in the structure of composite material. This can result in a shorter mean free path of the phonons and consequently a reduction in thermal conductivity as reported by Wang et al. [39]. Therefore, we expect a significant increase in the figure of merit, ZT. On the other hand, due to the ductile nature of the silver (Ag) metal Ag, we also expect an improvement in the mechanical properties of composite materials, in particular in terms of toughness.

Moreover, this study demonstrates that we can also use the SPT to texture other layered materials such as  $\text{Bi}_2\text{Sr}_2\text{Ca}_2\text{Cu}_3\text{O}_{10}$  (Bi2223) superconductor. The 98%-dense and highly textured Bi2223 sample were obtained with a magnetic anisotropy factor of 3.

At this stage of the study, there is further scope for improving the various parameters of the process: applied pressure, length and temperature of the dwell, controlled atmosphere, etc. to result in samples with improved efficiency.

**Author Contributions:** Y.X. was in charge of superconducting part, material preparation and characterizations; J.G.N. supervised this work and took in charge of thermoelectric part from material preparation to the properties studies. All authors have read and agreed to the published version of the manuscript.

**Funding:** This research received no external funding.

**Institutional Review Board Statement:** Not applicable.

**Informed Consent Statement:** Not applicable.

**Data Availability Statement:** Data available in a publicly accessible repository.

**Acknowledgments:** Y.X. acknowledges a fellowship from Conseil Régional de Normandie, France. The authors thank J. Lecourt and C. Bilot for their relevant technical supports.

**Conflicts of Interest:** The authors declare no conflict of interest.

## References

1. Bednorz, J.G.; Müller, K.A. Possible High T<sub>c</sub> Superconductivity in the Ba-La-Cu-O System. *Phys. B Condens. Matter* **1986**, *64*, 189. [[CrossRef](#)]
2. Jin, S.; Tiefel, T.H.; Sherwood, R.C.; van Dover, R.B.; Davis, M.E.; Kammlott, G.W.; Fastnacht, R.A. Melt-textured growth of polycrystalline  $\text{YBa}_2\text{Cu}_3\text{O}_{7-\delta}$  with high transport J, at 77 K. *Phys. Rev. B* **1988**, *37*, 7850–7853. [[CrossRef](#)]
3. de Rango, P.; Lees, M.R.; Lejay, P.; Sulpice, A.; Tournier, R.; Ingold, M.; Germi, M.; Pernet, M. Texturing of magnetic materials at high temperature by solidification in a magnetic field. *Nature* **1991**, *349*, 770–772. [[CrossRef](#)]
4. Lees, M.R.; de Rango, P.; Bourgault, D.; Barbut, J.M.; Braithwaite, D.; Lejay, P.; Sulpice, A.; Tournier, R. Bulk textured rare earth- $\text{Ba}_2\text{Cu}_3\text{O}_{7-\delta}$  prepared by solidification in a magnetic field. *Supercond. Sci. Technol.* **1992**, *5*, 362–367. [[CrossRef](#)]
5. Dou, S.X.; Liu, H.K.; Apperley, M.H.; Sing, K.H.; Sorrell, C.C.; Easterling, K.E.; Niska, J.; Guo, S.J. Improvement of critical current density in the Bi-Pb-Sr-Ca-Cu-O system through hot isostatic pressing. *Phys. C* **1990**, *167*, 525–528. [[CrossRef](#)]
6. Seino, H.; Ishizaki, K.; Takata, M. HIPped high density Bi-(Pb)-Sr-Ca-Cu-O superconductors produced without any additional treatment. *Jpn. J. Appl. Phys.* **1989**, *28*, L78–L81. [[CrossRef](#)]
7. Miller, D.J.; Sengupta, S.; Hettinger, J.D.; Shi, D.; Gray, K.E. Flux pinning in hot isostatically pressed  $\text{Bi}_2\text{Sr}_2\text{CaCu}_2\text{O}_x$ . *Appl. Phys. Lett.* **1992**, *61*, 2823–2825. [[CrossRef](#)]
8. Assano, T.; Tanaka, Y.; Fukutomi, M.; Jikihara, K.; Maeda, H. Properties of Pb-Doped Bi-Sr-Ca-Cu-O Superconductors Prepared by the Intermediate Pressing Process. *Jpn. J. Appl. Phys.* **1989**, *28*, L595–L597. [[CrossRef](#)]
9. Gao, W.; Sande, J.B.V. Textured BSCCO/Ag superconducting microcomposites with improved critical current density through mechanical deformation. *Supercond. Sci. Technol.* **1992**, *5*, 318–326. [[CrossRef](#)]
10. Ichinose, N.; Saito, K. Grain orientation of the Bi-Sr-Ca-Cu-O system ceramics by hotforging and their superconducting properties. *Phys. C* **1991**, *190*, 177–179. [[CrossRef](#)]
11. Terasaki, I.; Sasago, Y.; Uchinokura, K. Large thermoelectric power in  $\text{NaCo}_2\text{O}_4$  single crystals. *Phys. Rev. B* **1997**, *56*, R12685. [[CrossRef](#)]
12. Masset, A.C.; Michel, C.; Maignan, A.; Hervieu, M.; Toulemonde, O.; Studer, F.; Raveau, B. Misfit-layered cobaltite with an anisotropic giant magnetoresistance:  $\text{Ca}_3\text{Co}_4\text{O}_9$ . *Phys. Rev. B* **2000**, *63*, 166. [[CrossRef](#)]

13. Zhou, Y.; Matsubara, I.; Horii, S.; Takeuchi, T.; Funahashi, R.; Shikano, M.; Shimoyama, J.; Kishio, K.; Shin, W.; Izu, N.; et al. Thermoelectric properties of highly grain-aligned and densified Co-based oxide ceramics. *J. Appl. Phys.* **2003**, *93*, 2653. [[CrossRef](#)]
14. Scherrer, H.; Scherrer, S. Bismuth telluride, Antimony telluride and their solid solutions. In *CRC Handbook of Thermoelectricity*; Rowe, D.M., Ed.; CRC Press: London, UK, 1995; p. 211.
15. Gonzalez, E.J.; Blendell, J.E.; Cline, J.P.; Ritter, J.J.; Maruthamuthu, P.; Nelson, E.H.; Horn, S.B. Texture development in Bi<sub>2</sub>Te<sub>3</sub> during hot forging. *J. Mater. Res.* **1998**, *13*, 766. [[CrossRef](#)]
16. Hervieu, M.; Boullay, P.; Michel, C.; Maignan, A.; Raveau, B. A New Family of Misfit Layered Oxides with Double Rock Salt Layers Bi<sub>x</sub>(A<sub>0.75±ε</sub>Bi<sub>0.25±ε</sub>O)<sub>(3+3x)/2</sub>MO<sub>2</sub>(A=Ca, Sr and M=Co, Cr). *J. Solid State Chem.* **1999**, *142*, 305. [[CrossRef](#)]
17. Xu, G.; Funahashi, R.; Shikano, M.; Matsubara, I.; Zhou, Y. Thermoelectric properties of Bi<sub>2.2-x</sub>Pb<sub>x</sub>Sr<sub>2</sub>Co<sub>2</sub>O<sub>y</sub> system. *J. Appl. Phys.* **2002**, *91*, 4344. [[CrossRef](#)]
18. Yamamoto, T.; Tsukada, I.; Uchinokura, K.; Takagi, M.; Tsubone, T.; Ichihara, M.; Kobayashi, K. Structural Phase Transition and Metallic Behavior in Misfit Layered (Bi,Pb)-Sr-Co-O System. *Jpn. J. Appl. Phys.* **2000**, *39*, 747. [[CrossRef](#)]
19. Fujii, T.; Terasaki, I.; Watanabe, T.; Matsuda, A. Large In-Plane Anisotropy on Resistivity and Thermopower in the Misfit Layered Oxide Bi<sub>2-x</sub>Pb<sub>x</sub>Sr<sub>2</sub>Co<sub>2</sub>O. *Jpn. J. Appl. Phys.* **2002**, *41*, 783. [[CrossRef](#)]
20. Funahashi, R.; Urata, S.; Sano, T.; Kitawaki, M. Enhancement of thermoelectric figure of merit by incorporation of large single crystals in Ca<sub>3</sub>Co<sub>4</sub>O<sub>9</sub> bulk materials. *J. Mater. Res.* **2003**, *18*, 1646. [[CrossRef](#)]
21. Tani, T.; Itahara, H.; Xia, C.; Sugiyama, J. Topotactic synthesis of highly-textured thermoelectric cobaltites. *J. Mater. Chem.* **2003**, *13*, 1865. [[CrossRef](#)]
22. Matsubara, I.; Funahashi, R.; Takeuchi, T.; Sodeoka, S. Thermoelectric properties of spark plasma sintered Ca<sub>2.75</sub>Gd<sub>0.25</sub>Co<sub>4</sub>O<sub>9</sub> ceramics. *J. Appl. Phys.* **2001**, *90*, 462. [[CrossRef](#)]
23. Noudem, J.G. A new process for lamellar texturing of thermoelectric Ca<sub>3</sub>Co<sub>4</sub>O<sub>9</sub> oxides by spark plasma sintering. *J. Eur. Ceram. Soc.* **2009**, *29*, 2659–2663. [[CrossRef](#)]
24. Noudem, J.G.; Kenfaui, D.; Chateigner, D.; Gomina, M. Toward the enhancement of thermoelectric properties of lamellar Ca<sub>3</sub>Co<sub>4</sub>O<sub>9</sub> by edge-free spark plasma texturing. *Scr. Mater.* **2012**, *66*, 258–260. [[CrossRef](#)]
25. Prevel, M.; Perez, O.; Noudem, J.G. Bulk textured Ca<sub>2.5</sub>(RE)<sub>0.5</sub>Co<sub>4</sub>O<sub>9</sub> (RE: Pr, Nd, Eu, Dy and Yb) thermoelectric oxides by sinter-forging. *Solid State Sci.* **2007**, *9*, 231. [[CrossRef](#)]
26. Oide, Y.; Miyazaki, Y.; Ono, Y.; Huang, X.Y.; Kajitani, T. Thermogravimetric Study and High-Temperature Thermoelectric Properties of [Ca<sub>2</sub>(Co<sub>1-x</sub>A<sub>x</sub>)O<sub>3</sub>]<sub>0.62</sub>CoO<sub>2</sub>. In Proceedings of the 2006 25th International Conference on Thermoelectrics, Vienna, Austria, 6–10 August 2006; pp. 402–405. [[CrossRef](#)]
27. Miyazaki, Y.; Miura, T.; Onoda, M.; Uchida, M.; Ishii, Y.; Ono, Y.; Morii, Y.; Kajitani, T. Modulated Structure of Misfit-Layered Cobalt Oxide [Ca<sub>2</sub>(Co<sub>0.65</sub>Cu<sub>0.35</sub>)<sub>2</sub>O<sub>4</sub>]<sub>0.63</sub>CoO<sub>2</sub>. *Jpn. J. Appl. Phys.* **2003**, *42*, 7467–7473. [[CrossRef](#)]
28. Liou, Y.C.; Tsai, W.C.; Lin, W.Y.; Lee, U.R. Synthesis of Ca<sub>3</sub>Co<sub>4</sub>O<sub>9</sub> and CuAlO<sub>2</sub> Ceramics of the Thermoelectric Application Using A Reaction-Sintering Proces. *J. Aust. Ceram. Soc.* **2008**, *44*, 17–22.
29. Rouessac, V.; Wang, J.; Provost, J.; Desgardin, G. Processing and superconducting properties of highly textured Bi(Pb)-2223 ceramics by sinter-forging. *Phys. C* **1996**, *268*, 225. [[CrossRef](#)]
30. Prevel, M.; Lemonnier, S.; Klein, Y.; Hébert, S.; Chateigner, D.; Ouladdiaf, B.; Noudem, J.G. Textured Ca<sub>3</sub>Co<sub>4</sub>O<sub>9</sub> thermoelectric oxides by thermo-forging process. *J. Appl. Phys.* **2005**, *98*, 093706-9. [[CrossRef](#)]
31. Kenfaui, D.; Lenoir, B.; Chateigner, D.; Ouladdiaf, B.; Gomina, M.; Noudem, J.G. Development of multilayer textured Ca<sub>3</sub>Co<sub>4</sub>O<sub>9</sub> materials for thermoelectric generators: Influence of the anisotropy on the transport properties. *J. Eur. Ceram. Soc.* **2012**, *32*, 2405–2414. [[CrossRef](#)]
32. Tang, G.D.; Guo, H.H.; Yang, T.; Zhang, D.W.; Xu, X.N.; Wang, L.Y.; Wang, Z.H.; Wen, H.H.; Zhang, Z.D.; Du, Y.W. Anisotropic thermopower and magnetothermopower in a misfit-layered calcium cobaltite. *Appl. Phys. Lett.* **2011**, *98*, 202109. [[CrossRef](#)]
33. Soret, J.; Lepetit, M. Electronic structure of the Ca<sub>3</sub>Co<sub>4</sub>O<sub>9</sub> compound from ab initio local interactions. *Phys. Rev. B* **2012**, *85*, 165145. [[CrossRef](#)]
34. Ren, W.L.; Li, C.C.; Zhang, L.T.; Ito, K.; Wu, J.S. Effects of Ge and B substitution on thermoelectric properties of CoSi. *J. Alloys Comp.* **2005**, *392*, 50. [[CrossRef](#)]
35. Asanabe, S.; Shinoda, D.; Sasaki, Y. Semimetallic Properties of Co<sub>1-x</sub>Fe<sub>x</sub>Si Solid Solutions. *Phys. Rev. A* **1964**, *134*, 774. [[CrossRef](#)]
36. Koshibae, W.; Tsutui, K.; Maekawa, S. Thermopower in cobalt oxides. *Phys. Rev. B* **2000**, *62*, 6869. [[CrossRef](#)]
37. Noudem, J.G.; Guilmeau, E.G.; Chateigner, D. Recent developments in processing and performance of hot stacked-sinter forged Bi2223 ceramics. *Phys. C* **2003**, *391*, 265. [[CrossRef](#)]
38. Guilmeau, E.; Noudem, J.G. Influence of the sinter-forging temperature on the superconducting properties of Bi2223 textured discs. *Supercond. Sci. Technol.* **2002**, *15*, 1566–1570. [[CrossRef](#)]
39. Wang, Y.; Sui, Y.; Cheng, J.; Wang, X.; Su, W. The thermal-transport properties of the Ca<sub>3-x</sub>Ag<sub>x</sub>Co<sub>4</sub>O<sub>9</sub> system (0 ≤ x ≤ 0.3). *J. Phys. Condens. Matter.* **2007**, *19*, 356216–356226. [[CrossRef](#)]